

# A disc reflection model for ultra-soft narrow-line Seyfert 1 galaxies

Jiachen Jiang<sup>1,2,3\*</sup>, Luigi C. Gallo,<sup>4</sup> Andrew C. Fabian<sup>1,3</sup>, Michael L. Parker<sup>1,5</sup>  
and Christopher S. Reynolds<sup>3</sup>

<sup>1</sup>*Tsinghua Center for Astrophysics, Tsinghua University, Shuangqing Road, Beijing 100084, China*

<sup>2</sup>*Department of Astronomy, Tsinghua University, Shuangqing Road, Beijing 100084, China*

<sup>3</sup>*Institute of Astronomy, University of Cambridge, Madingley Road, Cambridge CB3 0HA, UK*

<sup>4</sup>*Department of Astronomy and Physics, Saint Mary's University, 923 Robie Street, Halifax, NS B3H 3C3, Canada*

<sup>5</sup>*European Space Agency, European Space Astronomy Centre, E-28691 Villanueva de la Cañada, Spain*

Accepted 2020 August 20. Received 2020 August 20; in original form 2019 November 6

## ABSTRACT

We present a detailed analysis of the *XMM–Newton* observations of five narrow-line Seyfert 1 galaxies (NLS1s). They all show very soft continuum emission in the X-ray band with a photon index of  $\Gamma \gtrsim 2.5$ . Therefore, they are referred to as ‘ultra-soft’ NLS1s in this paper. By modelling their optical/UV–X-ray spectral energy distribution (SED) with a reflection-based model, we find indications that the disc surface in these ultra-soft NLS1s is in a higher ionization state than other typical Seyfert 1 AGN. Our best-fitting SED models suggest that these five ultra-soft NLS1s have an Eddington ratio of  $\lambda_{\text{Edd}} = 1\text{--}20$  assuming available black hole mass measurements. In addition, our models infer that a significant fraction of the disc energy in these ultra-soft NLS1s is radiated away in the form of non-thermal emission instead of the thermal emission from the disc. Due to their extreme properties, X-ray observations of these sources in the iron band are particularly challenging. Future observations, e.g. from *Athena*, will enable us to have a clearer view of the spectral shape in the iron band and thus distinguish the reflection model from other interpretations of their broad-band spectra.

**Key words:** accretion, accretion discs – black hole physics – galaxies: Seyfert – X-rays: galaxies.

## 1 INTRODUCTION

Narrow-line Seyfert 1 galaxies (NLS1s) are a unique class of Seyfert 1 galaxies (Sy1s). They are similar to other Sy1s, except for having strong Fe II emission, weak [O III] emission, and a narrow H  $\beta$  line (e.g. Osterbrock & Phillips 1977; Goodrich 1989). According to the definition of NLS1, the full width at half-maximum (FWHM) of their H  $\beta$  lines is smaller than  $5000 \text{ km s}^{-1}$  (Goodrich 1989). These narrow H  $\beta$  lines are believed to be related to the small black hole (BH) masses in NLS1s, assuming H  $\beta$  emission is related to the broad-line region (BLR; Grupe & Mathur 2004). However, Marconi et al. (2008) points out that NLS1s and other Sy1s may have similar BH masses if the radiation pressure on to the BLR is taken into account. This is particularly important in NLS1s, where the disc is often found to have a near-Eddington accretion rate.

In the X-ray band, NLS1s often show unique properties, such as very soft continuum emission and highly variable soft excess emission (e.g. Boller, Brandt & Fink 1996; Gallo 2018). Gallo (2006) classifies NLS1s into two general categories according to the variability of their optical and X-ray emission: ‘complex’ and ‘simple’ NLS1s. ‘Complex’ NLS1s often show larger X-ray flux variability than the ‘simple’ ones. For example, 1H 0707–495 and IRAS 13224–3809, classified as ‘complex’ NLS1s, show very fast and large flux variability on kilosecond time-scales (e.g. Boller et al. 2003; Fabian et al. 2004; Alston et al. 2019). The X-ray complexity of these NLS1s is often explained by either the light-bending model

in the reflection scenario (e.g. Miniutti 2006; Jiang et al. 2019b), or variable ionized absorption fully or partially covering the central emission region (e.g. Done & Jin 2016). It is important to mention the increasing number of discoveries of X-ray reverberation lags. They are seen in the soft X-ray band (e.g. Fabian et al. 2009; De Marco et al. 2013), the iron band (e.g. Kara et al. 2016), and the hard X-ray band (e.g. Zoghbi et al. 2014; Kara et al. 2015) of some AGNs that have no obvious evidence of strong ionized absorption features in their spectra. In addition, detailed principle component analysis also shows that the X-ray variability agrees with the reflection scenario in these unabsorbed sources (Parker et al. 2014, 2015). Similar X-ray reverberation lags and spectral properties have also been seen in BH X-ray binaries (e.g. Reis et al. 2013; De Marco et al. 2015; Kara et al. 2019; Mastroserio, Ingram & van der Klis 2019).

In this work, we present detailed spectral analysis for five extreme NLS1s: RBS 2041, RX J0439.6–5311, RX J0136.9–3510, RX J1355.2+5612, and 1ES 0919+515. See Table 1 for further information about them. These sources have been identified in the *ROSAT* soft X-ray survey (Voges et al. 1999). They show extremely soft emission in the soft X-ray band, and potentially host a BH that is accreting around or above the Eddington limit. Due to the extreme steepness of their X-ray spectra, we refer them as ultra-soft NLS1s in this paper. The high accretion rates of these ultra-soft NLS1s are particularly interesting. For instance, we might be able to understand the existence of massive quasars in the early universe by studying these nearby sources (e.g. Wu et al. 2015; Bañados et al. 2016, 2018; Tang et al. 2019).

Previously, the soft X-ray emission from these ultra-soft NLS1s was modelled by warm corona models, where there is an optically

\* E-mail: jcjiang@mail.tsinghua.edu.cn

**Table 1.** List of *XMM-Newton* observations analysed in this work. The redshift values are from the NED website. The last column shows the net exposure of MOS1, MOS2, and pn observations, respectively, after removing the time intervals that are dominated by flaring particle background. Column 3: The BH masses were estimated by measuring  $H\beta$  line widths. Column 4: References for  $M_{\text{BH}}$  measurements.

Source	Full name	$M_{\text{BH}}$ ( $10^6 M_{\odot}$ )	Ref	$z$	$N_{\text{H}}$ ( $10^{20} \text{ cm}^{-2}$ )	$E(B - V)$	Obs ID	Net exposure (ks)
RBS 2041	RBS 2041	10	Grupe et al. (2010)	0.137	2.16	0.029	0741390301	34, 34, 28
RX J0439	RX J0439.6–5311	3.9	Grupe et al. (2010)	0.243	0.82	0.006	0741390101 0764530101	25, 25, 18 131, 130, 122
RX J0136	RX J0136.9–3510	79	Jin et al. (2009)	0.289	2.17	0.018	0303340101	50, 50, 38
RX J1355	RX J1355.2+5612	6.7	Grupe et al. (2010)	0.122	1.05	0.010	0741390201 0741390401	23, 23, 16 22, 26, 19
1ES 0919	1ES 0919+515	5.0	Komossa et al. (2008)	0.159	1.37	0.014	0300910301	23, 23, 4

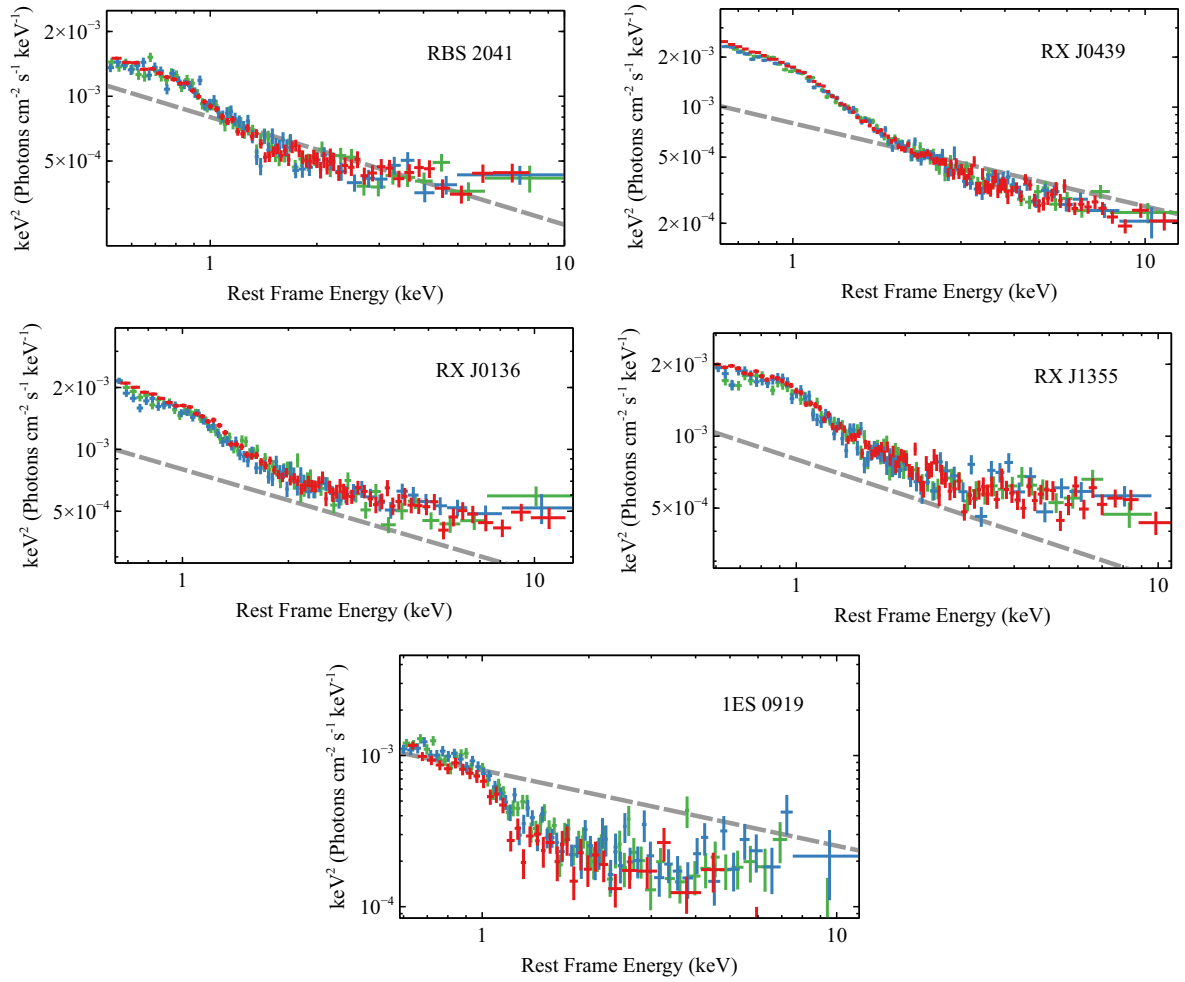


**Figure 1.** Unfolded spectra of the five NLS1s in our work. Red: pn; blue: MOS1; green: MOS2. A power-law model with  $\Gamma = 0$  is used to unfold the spectra. The dashed grey line in each panels show a power law with  $\Gamma = 2.5$  in comparison with the data.

thick corona in addition to the optically thin hot corona (e.g. Jin et al. 2009, 2017). The temperature of this extra corona is usually below 1 keV (Jin et al. 2012; Petrucci et al. 2018; Panda et al. 2019), which is much lower than the hot corona. Therefore, they are often referred to as the ‘warm’ corona. In this scenario, the UV emission from ultra-soft NLS1s was often found to be dominated by this warm coronal emission instead of the thermal emission from the disc, and the discs were found to accrete at a super-Eddington accretion rate of more than 10 times the Eddington limit (e.g. Jin et al. 2009).

An alternative explanation of soft excess emission is the reflection from the innermost region of the accretion disc (e.g. Crummy et al. 2006; Walton et al. 2013; Jiang et al. 2019a). In this scenario, the disc is illuminated by the non-thermal emission from the hot corona, and produces reprocess spectrum within the Thomson optical depth of the disc. The reprocess spectrum is referred to as the disc ‘reflection’ spectrum, which consists of series of emission lines in the soft X-ray band and a Compton back-scattered continuum in the hard X-ray band (e.g. Ross & Fabian 1993; García & Kallman 2010).

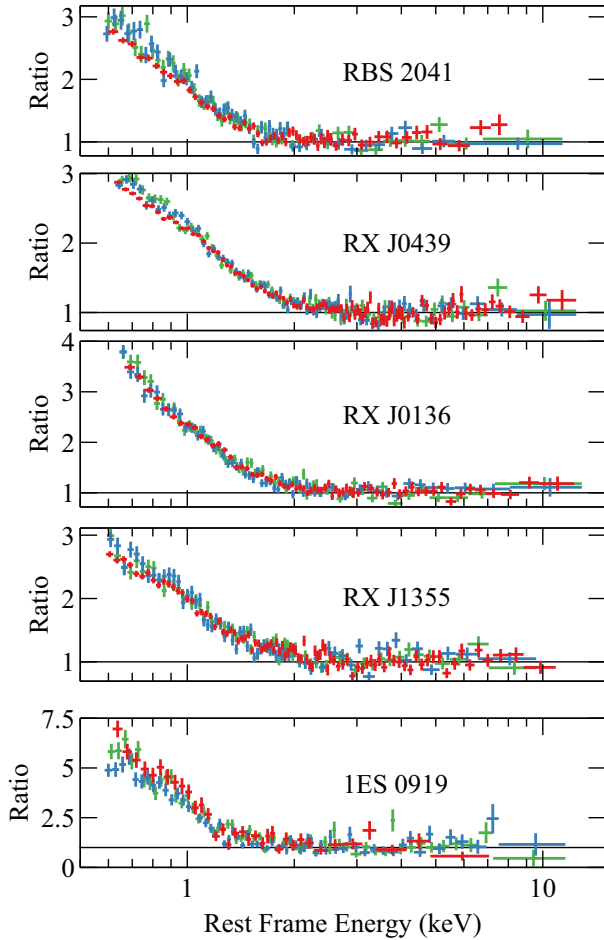


**Figure 2.** Data/model ratio plots using the best-fitting absorbed power-law models for the spectra above 2 keV.

The emission lines are broadened by strong relativistic effects in the vicinity of BHs (e.g. Reynolds 2019).

In this paper, we systematically apply this relativistic disc reflection model to the *XMM-Newton* data of five ultra-soft NLS1s, and study their broad-band spectral energy distribution (SED) based on our reflection modelling. In Section 2, we introduce the data reduction process. In Section 3, we analyse the X-ray spectra of these sources by using disc reflection model. We also show supporting MCMC analysis of the X-ray data in Appendix A. In Section 4, we model their SEDs by extending our reflection model to the optical and UV bands. In Section 5, we summarize our results.

## 2 XMM-NEWTON DATA REDUCTION

We use the European Photon Imaging Camera (EPIC) observations for X-ray continuum modelling, and the optical monitor (OM) observations for flux measurements in the optical and UV bands. A full list of observations used in our work is in Table 1.

The EPIC data are reduced using V17.0.0 of the *XMM-Newton* Science Analysis System (SAS) software package. The version of the calibration files is v.20180620. We first generate a clear event file by running EMPROC (for EPIC-MOS data) and EPPROC (for EPIC-pn data). Then, we select good time intervals by filtering out the intervals that are dominated by flaring particle background. These high-background intervals are where the single event

(PATTERN=0) count rate in the  $>10$  keV band is larger than  $0.35 \text{ counts s}^{-1}$  ( $0.4 \text{ counts s}^{-1}$ ) for MOS (pn) data. By running the EVSELECT task, we select single and double events for EPIC-MOS (PATTERN $\leq 12$ ) and EPIC-pn (PATTERN $\leq 4$ , FLAG==0) source event lists from a circular source region. No obvious evidence of pile-up effects has been found in our observations. The background spectra are extracted from nearby regions on the same unit. Last, we create redistribution matrix files and ancillary response files by running RMFGEN and ARFGEN.

We consider the EPIC spectra between 0.5 and 10 keV. The EPICSPECCOMBINE tool is used to make a stacked spectrum for each camera, along with corresponding background spectra and response matrix files, if there are multiple observations for one source. We do not merge spectra from different instruments. The SPECGROUP command is used to group the spectra such that each bin has a minimum number of 20 counts and a minimum width that is  $1/3$  of the resolution at that energy.

We reduce OM data using the OMICHAIN tool. In order to convert the flux obtained by OM into the XSPEC data format, we apply the OM2PHA tool to the combined source list of each observation. The corresponding OM response files can be found on the *XMM-Newton* website.<sup>1</sup>

## 3 X-RAY SPECTRAL ANALYSIS

We use XSPEC V12.10.1h (Arnaud 1996) for spectral analysis, and  $\chi^2$  is considered in this work. The column density of the Galactic absorption along the line of sight towards our sources is calculated by Willingale et al. (2013), which can be found in Table 1. The tbnew model (Wilms, Allen & McCray 2000) is used to account for Galactic absorption, and the zdust model (Pei 1992) is used to account for Galactic extinction. We fix the column density of the Galactic absorption at the values given by Willingale et al. (2013) during our spectral fitting as they are all very low and cannot be constrained by our data. The luminosity distances of our sources are from the NED website, where  $H_0 = 67.8 \text{ km s}^{-1} \text{ Mpc}^{-1}$ ,  $\Omega_{\text{matter}} = 0.308$ , and  $\Omega_{\text{vacuum}} = 0.692$  are assumed.

### 3.1 Reflection model setup

All the X-ray spectra analysed in our work are shown in Fig. 1. They are unfolded using a power-law model with  $\Gamma = 0$  to remove the impact of instrumental response. The grey line in each panel shows a power-law model with  $\Gamma = 2.5$  and the same normalization for comparison between the data. At the first glance, all the spectra show a continuum softer than  $\Gamma = 2.5$  below 3 keV, and turn harder above 3 keV. But the steepness of the spectra is slightly different in different sources. For example, the spectra of RX J0439 are consistent with  $\Gamma = 2.5$  above 3 keV. In comparison, the spectra of 1ES 0919 are relatively harder, and are consistent with a power law with  $\Gamma = 2$  above 3 keV.<sup>2</sup>

We first model all the spectra above 2 keV with an absorbed power-law model, and then include the 0.5–2 keV band of the spectra without changing the fits. The data/model ratio plots are shown in Fig. 2.

In the soft X-ray band, all the spectra show very steep ‘excess’ emission below 2 keV. The signal to noise (S/N) in the iron band of our observations is too low due to the steepness of the intrinsic spectra

<sup>1</sup>[ftp://xmm.esac.esa.int/pub/ccf/constituents/extras/responses/OM](http://xmm.esac.esa.int/pub/ccf/constituents/extras/responses/OM)

<sup>2</sup>A power law with  $\Gamma = 2$  would be a horizontal line in this figure.

**Table 2.** Best-fitting parameters for all the sources.  $F_{\text{refl}}$  and  $F_{\text{pl}}$  are the fluxes of the best-fitting reflection and Comptonization models in the 0.5–10 keV band. The reflection fraction  $f_{\text{refl}}$  is defined as  $F_{\text{refl}}/F_{\text{pl}}$ .  $F_{0.5-2 \text{ keV}}$  and  $F_{2-10 \text{ keV}}$  is the absorption-corrected X-ray flux in the 0.5–2 and 2–10 keV bands, respectively.

Model	Parameter	Unit	RBS 2041	RX J0439	RX J0136	RX J1355	1ES 0919
relconv	$q$		$>4$	$2.8^{+1.5}_{-1.2}$	$4^{+3}_{-2}$	$>5$	$4^{+4}_{-2}$
	$i$	deg	$35^{+12}_{-7}$	$>70$	$30^{+15}_{-7}$	$60^{+12}_{-22}$	$42^{+12}_{-4}$
	$a_*$		$0.4^{+0.5}_{-0.9}$	$>0.8$	$>0.88$	$>0.5$	Unconstrained
reflionx	$Z_{\text{Fe}}$	$Z_{\odot}$	$2 \pm 0.5$	$1.0 \pm 0.2$	$1.3 \pm 0.2$	$2.0 \pm 0.2$	$1.7^{+0.3}_{-0.2}$
	$\log(\xi)$	$\log(\text{erg cm s}^{-1})$	$3.18^{+0.12}_{-0.10}$	$3.01^{+0.08}_{-0.10}$	$3.19^{+0.04}_{-0.15}$	$3.3^{+0.10}_{-0.07}$	$2.6^{+0.22}_{-0.12}$
	$\log(n_e)$	$\log(\text{cm}^{-3})$	$<15.4$	$17.5 \pm 0.2$	$<15.6$	$<16.2$	$16.6^{+0.5}_{-0.4}$
	$\log(F_{\text{refl}})$	$\log(\text{erg cm}^{-2} \text{ s}^{-1})$	$-11.72^{+0.09}_{-0.07}$	$-11.65 \pm 0.03$	$-11.68 \pm 0.03$	$-11.70 \pm 0.06$	$-11.957^{+0.017}_{-0.018}$
nthcomp	$\Gamma$		$2.50 \pm 0.02$	$2.521^{+0.020}_{-0.012}$	$2.57 \pm 0.02$	$2.490^{+0.003}_{-0.002}$	$2.48 \pm 0.02$
	$\log(F_{\text{pl}})$	$\log(\text{erg cm}^{-2} \text{ s}^{-1})$	$-11.74 \pm 0.02$	$-11.65 \pm 0.03$	$-12.15 \pm 0.08$	$-11.68 \pm 0.04$	$-12.26^{+0.07}_{-0.08}$
constant	MOS1		1	1	1	1	1
	MOS2		$1.000 \pm 0.013$	$1.006 \pm 0.011$	$1.014 \pm 0.011$	$0.997^{+0.019}_{-0.013}$	$1.00 \pm 0.03$
	pn		$0.949 \pm 0.010$	$0.975 \pm 0.008$	$0.997 \pm 0.009$	$0.972^{+0.013}_{-0.007}$	$0.78 \pm 0.03$
	$f_{\text{refl}}$		1.1	4.5	3.0	1.0	2.0
	$F_{0.5-2 \text{ keV}}$	$10^{-12} \text{ erg cm}^{-2} \text{ s}^{-1}$	2.69	2.32	2.33	2.77	1.33
	$F_{2-10 \text{ keV}}$	$10^{-12} \text{ erg cm}^{-2} \text{ s}^{-1}$	1.01	0.48	0.74	1.11	0.34
	$\chi^2/\nu$		345.91/297	471.20/380	337.58/325	453.22/337	174.62/148

and the brightness of AGNs. Therefore, we are unable to determine the existence of broad Fe K emission with high confidence.

However, it is important to mention that the lack of evidence for ‘apparent’ broad Fe K emission line in limited S/N data does not rule out the existence of a reflection spectrum from the inner disc in unobscured Seyfert AGN especially when strong soft excess emission is found. The weak broad iron lines could be due to certain disc properties (e.g. a high-ionization state, García et al. 2013), extreme relativistic effects near a spinning BH (e.g. Crumey et al. 2006) and the very soft nature of the X-ray emission. Future high S/N soft X-ray observations, e.g. from *Athena*, will be able to obtain a more detailed view of these ultra-soft NLS1s in the iron band. See Section 5 for simulations for future *Athena* observations based on our reflection model.

Secondly, we model the full-band spectra by including both disc reflection and coronal emission. The *nthcomp* model (Życki, Done & Smith 1999) is used to model the continuum emission from the hot corona. This model calculates the thermal Comptonization process of cool disc seed photons in a hot coronal region. The electron temperature ( $kT_e$ ) of the corona decides the high-energy cut-off of the spectrum. We fix this parameter at  $kT_e = 100 \text{ keV}$  during our fit due to the lack of simultaneous hard X-ray data. A disc-blackbody spectrum is assumed for seed photons. The low-energy turnover, which is determined by the disc seed photon temperature  $kT_{\text{db}}$ , is not visible in the X-ray data. Therefore, we fix this parameter at  $kT_{\text{db}} = 10 \text{ eV}$  when analysing our X-ray spectra.

An extended version of the *reflionx* model (Ross & Fabian 1993) is used in our work,<sup>3</sup> which calculates the reprocess spectrum from an ionized slab illuminated by *nthcomp* (Jiang et al., submitted). We link the  $kT_{\text{db}}$ ,  $kT_e$ , and  $\Gamma$  parameters in *reflionx* to the corresponding parameters in *nthcomp*. Other

parameters in *reflionx* are the disc iron abundance ( $Z_{\text{Fe}}$ ), the disc ionization ( $\xi$ ), and the density of the disc within the optical depth ( $n_e$ ). The *relconv* model (Dauser et al. 2013) is applied to *reflionx* to account for relativistic correction. A phenomenological power-law disc emissivity profile parametrized by the index  $q$  is used for simplicity. The other parameters in *relconv* are the disc inclination angle ( $i$ ) and the BH spin parameter ( $a_*$ ). The inner radius of the disc is assumed to be at the Innermost Stable Circular Orbit (ISCO). The constant model is used to account for cross-calibration uncertainty between different instruments. The *cflux* model is used to calculate the flux of each component between 0.5 and 10 keV in the observer’s frame. The full model is `constant * tbnew* zdust * (cflux*relconv*reflionx + cflux*nthcomp)` in the XSPEC format. An empirical definition of reflection fraction is used here to compare the relative strength of the disc reflection component:  $f_{\text{refl}} = F_{\text{refl}}/F_{\text{pl}}$ , where  $F_{\text{refl}}$  and  $F_{\text{pl}}$  are the 0.5–10 keV band flux of the best-fitting *reflionx* and *nthcomp* models. Note that this reflection fraction is different from the physical definition of reflection fraction in Dauser et al. (2016).

We also test for any possible narrow Fe K emission line feature from a distant cold neutral reflector by adding an additional *xillver* model. The ionization parameter is fixed at  $\log(\xi) = 0$ . The fits between 3 and 10 keV of all of our six sources are not significantly improved. For example, RBS 2041 with  $\Delta\chi^2 = 4$  and 2 more free parameters. Only an upper limit of the normalization parameter of *xillver* is obtained ( $\text{norm} < 4 \times 10^{-6}$ ). Therefore, we conclude that there is no significant evidence for a distant reflector.

### 3.2 Results

The relativistic disc reflection model offers a very good fit for all of our X-ray spectra. The best-fitting parameters can be found in Table 2. The best-fitting models and corresponding data/model ratio plots can be found in Fig. 3. There are no obvious structural residuals after fitting the X-ray spectra with disc reflection model.

<sup>3</sup>We do not use the *relxill* model (García et al. 2016), which is another relativistic reflection model commonly used for spectral modelling. Because the publicly available version of *relxill* does not include the reflection spectrum below 0.1 keV. We need a consistent model to account for the non-thermal component in the later broad-band SED modelling.

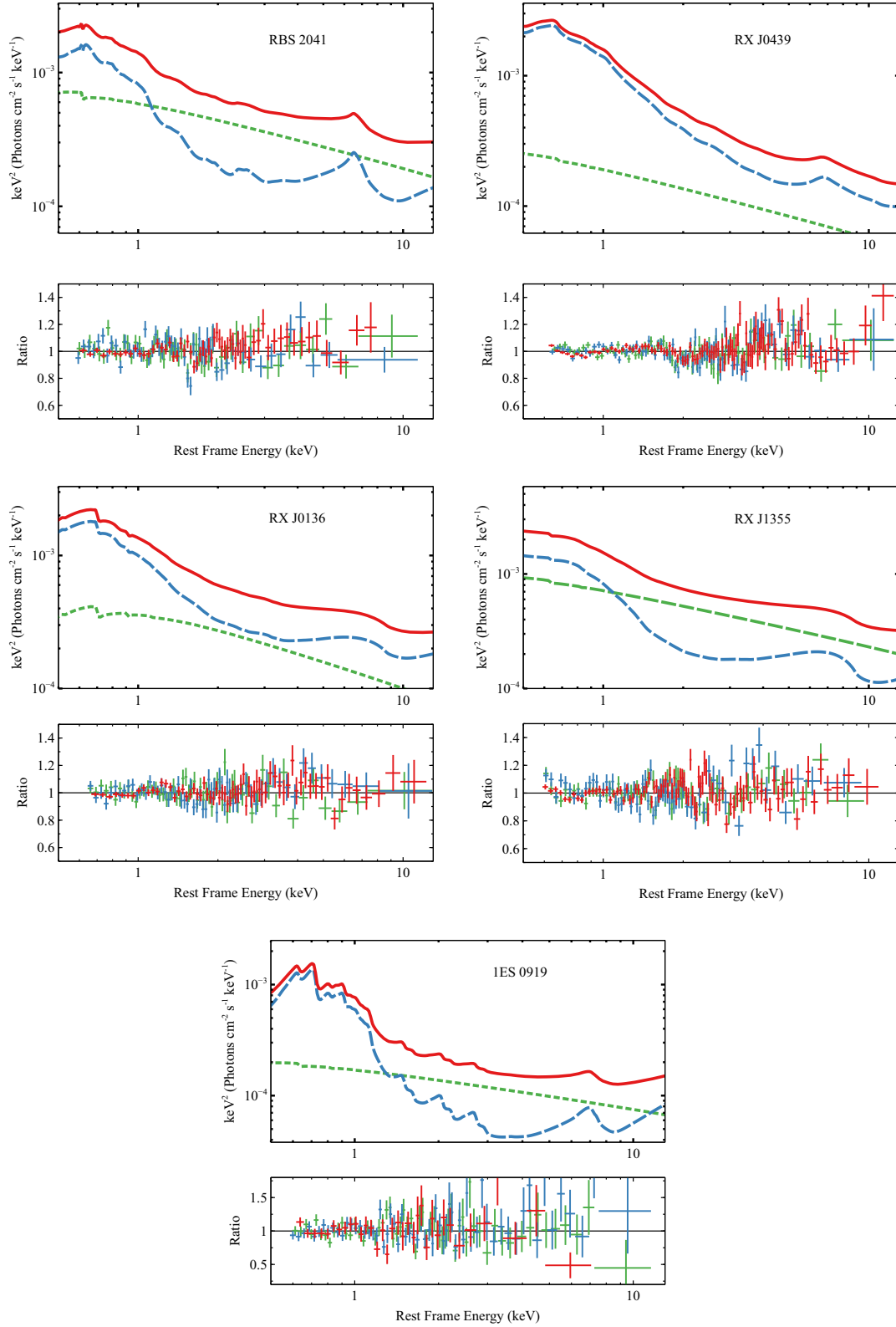


**Figure 3.** Best-fitting reflection models and corresponding data/model ratio plots. Red solid lines: total model; blue dashed lines: relativistic disc reflection; green dashed line: Comptonization model; red crosses: pn; blue crosses: MOS1; green crosses: MOS2.

We note that RX J0439 shows some excess emission above 9 keV in the source frame (see the second panel of Fig. 3), which was also noticed in the previous reflection modelling in Jin et al. (2017). By adding a weak hard power law to account for possible jet emission

as suggested in Jin et al. (2017), the fit is improved above 9 keV with  $\Delta\chi^2 = 5$  and 2 more free parameters. Jet emission is considered for many other RQ NLS1 (e.g. Wilkins et al. 2017) and could be distinguished with analysis of lag-frequency spectra (e.g. Alston



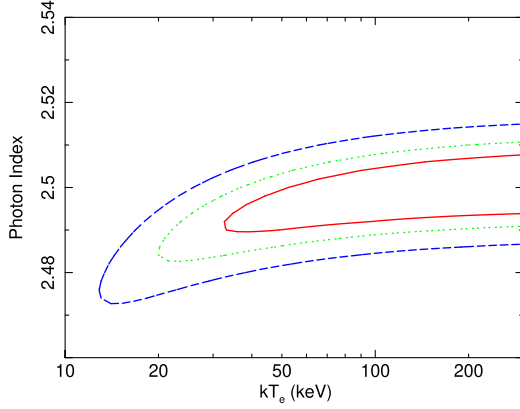


**Figure 4.** A contour plot of  $\chi^2$  distribution on the photon index versus  $kT_e$  parameter plane for RBS 2041. The lines show the  $1\sigma$  (red solid line),  $2\sigma$  (green dotted line), and  $3\sigma$  contours (blue dashed line). Only a lower limit of the coronal temperature is obtained. See text for more details.

et al. 2020) and emissivity profiles (Gonzalez, Wilkins & Gallo 2017). The key parameters of the reflection model for RX J0439 do not change after adding this additional power law. Therefore, we conclude that the excess feature is statistically insignificant. Another explanation of this feature is possible calibration uncertainty near the edge of the energy range of EPIC. This feature was not observed in other observations, which might be due to different configurations of the instrument when they were being operated. For instance, the EPIC-pn observation (obs ID 0764530101) of RX J0439 was the only one in our sample that was operated in the Large Window mode.

We test whether a distant reflector without relativistic blurring is able to explain the broad-band X-ray spectra. The convolution model `relconv` is removed for this test. Such a model provides a much worse fit as the model predicts narrow emission lines that are not shown in the CCD-resolution spectra. For instance, a distant reflector model offers a fit for RBS 2041 with  $\chi^2/\nu = 427.78/300$ . The relativistic reflection model is able to offer a much better fit with  $\Delta\chi^2 = 181.09$  and 3 more free parameters. Similar conclusions are found for other sources.

Additionally, we discuss the impact of the electron temperature of the corona ( $kT_e$ ) on our X-ray spectral modelling.  $kT_e$  determines the high-energy cut-off of the X-ray spectrum. This is particularly interesting as the X-ray continuum emission is very soft in ultra-soft

NLS1s. We fix this parameter at a large value ( $kT_e = 100$  keV) during the analysis above. In order to estimate how the  $kT_e$  parameter would affect our measurements of photon index, we allow this parameter to be free in the following test. For example, a  $\chi^2$  distribution on the  $\Gamma$  versus  $kT_e$  parameter plane for RBS 2041 is shown in Fig. 4. Due the lack of hard X-ray observations, we only obtain a lower limit of  $kT_e$ . The  $3\sigma$  lower limit is approximately 15 keV. The photon index has a  $3\sigma$  uncertainty range of  $\Gamma = 2.475$ – $2.495$  when  $kT_e = 20$  keV. In comparison,  $\Gamma = 2.48$ – $2.51$  when  $kT_e = 100$  keV. Although a slightly harder continuum is suggested when  $kT_e$  is low, measurements of  $\Gamma$  are consistent within a  $3\sigma$  uncertainty range for different values of  $kT_e$ . Similar conclusions are achieved for other sources.

Furthermore, we run Markov chain Monte Carlo (MCMC) analysis in addition to the  $\chi^2$  fit-goodness analysis in XSPEC in order to check any possible parameter degeneracy in our reflection model. Details can be found in Appendix A. The MCMC results are consistent with the uncertainty measurements given by the `ERROR` command in XSPEC.

We discuss the results of our X-ray spectral analysis as following:

(i) The BH spin parameter  $a_*$  is not well constrained in all five sources due to the lack of a clear view of the iron band in our spectra. The tightest constraint of  $a_*$  is for RX J0136 ( $a_* > 0.88$ ). However, our analysis shows that all five sources are statistically consistent with a rapidly spinning BH, e.g.  $a_* = 0.9$ . Similarly, the disc inclination is not well constrained neither by the data. Most sources have an inclination angle that is consistent with either a low value ( $i \approx 30^\circ$ ) or a high value ( $i \approx 60^\circ$ ) within a  $3\sigma$  uncertainty range. RX J0439 is the only case where our reflection model indicates an edge-on accretion disc with  $i > 70^\circ$ .

(ii) All five sources show a very high reflection fraction with  $f_{\text{refl}} \geq 1$ , which suggests that the reflection component makes a significant contribution to the X-ray flux. No supersolar iron abundance is found. It is also interesting to note that all of our sources show a higher disc ionization state than a typical Sy1 AGN [e.g.  $\log(\xi) = 1$ – $2$ ; Walton et al. 2013]. We only obtain an upper limit of the disc density parameter for RBS 2041, RX J0136, and RX J1355, which are all consistent with  $n_e = 10^{15} \text{ cm}^{-3}$ . RX J0439 and 1ES 0919 are found to have a moderate disc density of  $n_e = 10^{16}$ – $10^{18} \text{ cm}^{-3}$ .

(iii) The coronal emission of all five sources has  $\Gamma \gtrsim 2.5$ , which is softer than the continuum emission in a typical Sy1. Such soft coronal emission is only seen in the highest flux state of some other NLS1s (Dauser et al. 2012; Jiang et al. 2018).

**Table 3.** The best-fitting parameters of the `diskbb` model given by SED modelling, and the flux of the thermal (disc emission) and non-thermal (coronal emission and disc reflection) components inferred by our model.  $F_{\text{tot}}$  and  $F_{\text{non-th}}$  are the flux of the total emission and the non-thermal emission, respectively, calculated in the 0.1 eV–100 keV band.  $F_{\text{tot}}^{\text{opt}}$  and  $F_{\text{non-th}}^{\text{opt}}$  are the flux of the same components calculated in the 1–10 eV band. All the flux values are in the units of  $10^{-11} \text{ erg cm}^{-2} \text{ s}^{-1}$ .  $f_{\text{non-th}}$  and  $f_{\text{non-th}}^{\text{opt}}$  are the percentages of non-thermal emission in the 0.1 eV–100 keV and 1–10 eV bands, respectively.  $\lambda_{\text{Edd}}$  is the Eddington ratio estimated by using  $F_{\text{tot}}$  and assuming  $m_{\text{BH}}$  in Table 1.

Source	$kT$ (eV)	Norm	$F_{\text{tot}}$	$F_{\text{non-th}}$	$f_{\text{non-th}}$ (per cent)	$F_{\text{tot}}^{\text{opt}}$	$F_{\text{non-th}}^{\text{opt}}$	$f_{\text{non-th}}^{\text{opt}}$ (per cent)	$\lambda_{\text{Edd}}$	$\chi^2/\nu$
RBS 2041	$9 \pm 1$	$(4.3 \pm 0.7) \times 10^8$	10.7	5.2	49	2.5	0.7	28	3.8	353.03/298
RX J0439	$19 \pm 1$	$(1.3 \pm 0.2) \times 10^7$	5.7	2.1	37	0.5	0.07	14	18.5	539.61/385
RX J0136	$6.20 \pm 0.09$	$(1.1 \pm 0.2) \times 10^7$	7.6	4.8	62	0.6	0.2	33	1.9	404.32/326
RX J1355	$2_{-1}^{+4}$	$(2.2 \pm 0.2) \times 10^{10}$	4.6	4.2	90	1.1	0.7	64	2.0	531.04/341
1ES 0919	$7_{-1}^{+2}$	$(4.4 \pm 0.1) \times 10^8$	4.0	1.7	43	0.9	0.06	7	4.1	263.45/152

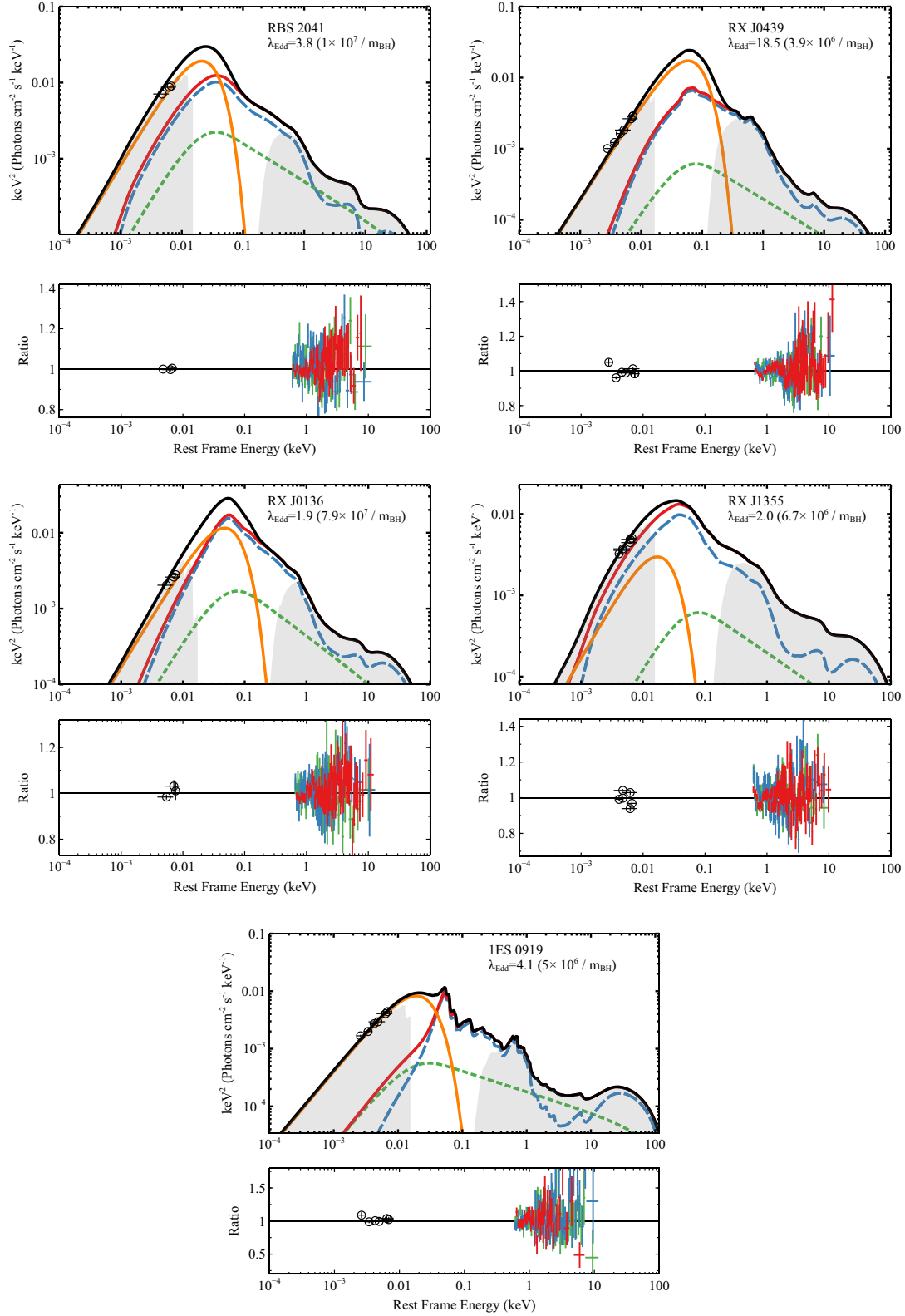


**Figure 5.** Top panels: SED models for all five ultra-soft NLS1s. Grey shaded regions: the best-fitting models; black solid lines: the best-fitting models after removing Galactic absorption and extinction; red solid lines: best-fitting non-thermal components after removing Galactic absorption and extinction, including relativistic disc reflection components (blue dashed lines) and thermal Comptonization components (green dashed lines); orange solid lines: disc thermal spectra. Bottom panels: corresponding data/model ratio plots. Red: pn; blue: MOS1; green: MOS2; black circles: OM. The error bars of OM points are smaller than the sizes of the points.

#### 4 SPECTRAL ENERGY DISTRIBUTION

So far we have obtained the best-fitting model for the X-ray data, which include coronal emission and disc reflection. We extend our X-ray model to the optical and UV band.

The thermal emission from the disc is consistently modelled by the disc-blackbody model `diskbb`. The  $kT_{\text{db}}$  parameter of the `diskbb` model is linked to the corresponding parameters in `reflionx` and `nthcomp`. The multiplicative model `zmshift` is applied to `diskbb` to account for the redshift. The full model is `constant * zdust * tbnew * (zmshift*diskbb + cflux*relconv*reflionx + cflux*nthcomp)` in the XSPEC format.

Note that we do not have the information about the host galaxies, such as the intrinsic dust extinction and the contribution of the star formation in the galaxies to the observed optical flux. But the combination of thermal (disc emission) and non-thermal (coronal emission and disc reflection) components can mostly describe the data very well. The best-fitting disc inner temperatures  $kT_{\text{db}}$  and the normalization parameters of `diskbb` for all sources are shown in Table 3. The other parameters listed in Table 2 are also allowed to vary during our SED modelling. These parameters show consistent values as in Table 3 and are sensitive to X-ray data only.

The best-fitting SED models are shown in Fig. 5, and the flux of the thermal and non-thermal components are shown in Table 3.  $F_{\text{th}}$  and  $F_{\text{non-th}}$  are the flux of the thermal and non-thermal components, respectively, in the 0.1 eV–100 keV band given by our best-fitting SED models.  $f_{\text{non-th}}$  is the flux ratio of the non-thermal emission and the total emission in the same energy band. Similarly,  $F_{\text{th}}^{\text{opt}}$ ,  $F_{\text{non-th}}^{\text{opt}}$ , and  $f_{\text{non-th}}^{\text{opt}}$  are calculated in the 1–10 eV band (optical and UV). The corresponding Eddington ratio  $\lambda = 4\pi D^2(F_{\text{th}} + F_{\text{non-th}})/L_{\text{Edd}}$  is labelled in each panel of Fig. 5 where  $L_{\text{Edd}}$  is calculated using the BH masses given in Table 1.

Assuming the BH mass measurements are all accurate, RX J0439 shows the highest Eddington ratio, which is approximately 19 times the Eddington limit, and RX J0136 shows the lowest Eddington ratio, which is around the Eddington limit. Our inferred Eddington ratios are similar to the values obtained by the warm corona models. For instance, Jin et al. (2009) found that the warm corona model suggests an Eddington ratio of  $\lambda_{\text{Edd}} \approx 2.7$  after adopting the same BH mass for RX J0136 as we do. However, our model predicts a higher fraction of disc thermal emission in the UV band. Readers may compare Fig. 5 with fig. 4 in Jin et al. (2009).

Note that RX J0136 and RX J0439 have a similar luminosity of  $1\text{--}2 \times 10^{46} \text{ erg s}^{-1}$ . The difference of their inferred Eddington ratios in our work is because RX J0136 was estimated to have a BH mass more than one order of magnitude higher than RX J0439 (e.g. Jin et al. 2009; Grupe et al. 2010). However, the systematic uncertainty of the BH mass measurements using  $H_{\beta}$  line width is very large, depending on the assumption for the geometry of the BLR [e.g.  $\Delta(\log(m_{\text{BH}})) = 0.5$ ; Kaspi et al. 2000; McLure & Dunlop 2004]. Moreover, the correction for radiation pressure on to the BLR may add more uncertainty to the mass measurements (Marconi et al. 2008). Therefore, they may share a similar Eddington ratio if RX J0136 and RX J0439 have a similar true BH mass. Nevertheless, we conclude that the five ultra-soft NLS1s in our sample share a similar bolometric luminosity and show an accretion rate around or a few times the Eddington limit.

It is interesting to mention that our best-fitting SED models suggest the non-thermal emission, including coronal emission and disc reflection, is responsible for more than 50 per cent of the total flux of RX J0439, RX J0136, and RX J1355 in the 0.1 eV–100 keV

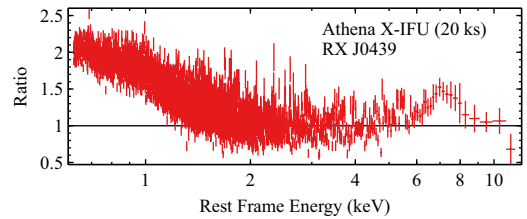


**Figure 6.** The data/model ratio plot for a simulated *Athena* X-IFU spectrum of RX J0439 using an absorbed power-law model. The simulations assume a net exposure of only 20 ks and are calculated using the best-fitting disc reflection model presented in Fig. 3. The spectrum has been grouped significantly for demonstration purposes.

band. The most extreme case is RX J1355, where the inferred non-thermal emission fraction is around 90 per cent in the full band and 64 per cent in the 1–10 eV (optical) band. The high fraction of non-thermal emission at longer wavelengths is due to the extremely soft coronal emission and the reflection from a highly ionized inner disc region.

Our results suggest that a significant fraction of disc energy in ultra-soft NLS1s is not radiated away from the disc surface as in the Shakura & Sunyaev (1973), but transferred to the coronal region and carried away in the form of non-thermal emission (Haardt & Maraschi 1991; Svensson & Zdziarski 1994).

#### 5 CONCLUSIONS

We analyse the *XMM-Newton* observations of five ultra-soft NLS1s using a relativistic disc reflection model in this work. A reflection-based SED model is able to describe the simultaneous OM and EPIC observations very well. Our reflection models indicate a more ionized disc in ultra-soft NLS1s compared to other typical Sy1s. The best-fitting SED models suggest that these sources share a similar luminosity, corresponding to an Eddington ratio of  $\lambda_{\text{Edd}} = 1\text{--}20$  assuming previous BH mass measurements. In particular, our models suggest that a significant fraction of the disc energy is carried away in the form of non-thermal emission instead of thermal emission from the surface of the disc. In the most extreme case, the optical emission of RX J1355 is dominated by non-thermal emission from the innermost region.

As explained above, the S/N of the *XMM-Newton* data in the iron band is not high enough to enable us to constrain the iron line profile due to the nature of these ultra-soft NLS1s: the broad-band spectral analysis by using a reflection model suggests that the disc density is low ( $n_e < 10^{18} \text{ cm}^{-3}$ ) and the ionization state is particularly high. At a high-ionization state [e.g.  $\log(\xi) > 3$ ], the surface of the disc becomes so ionized that the emission and absorption features in the reflection spectrum become very weak (Ross & Fabian 1993; García & Kallman 2010). Additionally, their ultra-soft X-ray continuum emission of  $\Gamma \approx 2.5$  makes their iron band observation particularly challenging.

Future observations with higher S/N and energy resolutions in the iron band, e.g. from *Athena*, will be able to better constrain the spectral shape in the iron band and thus distinguish the reflection interpretation from other models, such as warm corona (e.g. Porquet et al. 2019; Ballantyne 2020). As an example, we present a simulated *Athena* IFU spectrum of RX J0439 with a net exposure of 20 ks in Fig. 6. The spectrum is calculated using the best-fitting model obtained in Section 3. According to our simulations, *Athena* will be able to detect not only strong soft excess emission but also clear



evidence for a broad Fe K emission line assuming the right reflection model.

## ACKNOWLEDGEMENTS

JJ acknowledges support by the Tsinghua Astrophysics Outstanding (TAO) Fellowship and the Tsinghua Shuimu Scholar Programme. ACF acknowledges support by the ERC Advanced Grant 340442. MLP is supported by European Space Agency (ESA) Research Fellowships.

## DATA AVAILABILITY

The data underlying this article are available in the High Energy Astrophysics Science Archive Research Center (HEASARC), at <https://heasarc.gsfc.nasa.gov>.

## REFERENCES

- Alston W. N. et al., 2019, *MNRAS*, 482, 2088  
 Alston W. N. et al., 2020, *Nat. Astron.*, 4, 597  
 Arnaud K. A., 1996, in Jacoby G. H., Barnes J., eds, ASP Conf. Ser. Vol. 101, Astronomical Data Analysis Software and Systems V. Astron. Soc. Pac., San Francisco, p. 17  
 Ballantyne D. R., 2020, *MNRAS*, 491, 3553  
 Bañados E. et al., 2016, *ApJS*, 227, 11  
 Bañados E. et al., 2018, *Nature*, 553, 473  
 Boller T., Brandt W. N., Fink H., 1996, *A&A*, 305, 53  
 Boller T., Tanaka Y., Fabian A., Brandt W. N., Gallo L., Anabuki N., Haba Y., Vaughan S., 2003, *MNRAS*, 343, L89  
 Crummy J., Fabian A. C., Gallo L., Ross R. R., 2006, *MNRAS*, 365, 1067  
 Dauser T. et al., 2012, *MNRAS*, 422, 1914  
 Dauser T., García J., Wilms J., Böck M., Brenneman L. W., Falanga M., Fukumura K., Reynolds C. S., 2013, *MNRAS*, 430, 1694  
 Dauser T., García J., Walton D. J., Eikmann W., Kallman T., McClintock J., Wilms J., 2016, *A&A*, 590, A76  
 De Marco B., Ponti G., Cappi M., Dadina M., Uttley P., Cackett E. M., Fabian A. C., Miniutti G., 2013, *MNRAS*, 431, 2441  
 De Marco B., Ponti G., Muñoz-Darias T., Nandra K., 2015, *ApJ*, 814, 50  
 Done C., Jin C., 2016, *MNRAS*, 460, 1716  
 Fabian A. C., Miniutti G., Gallo L., Boller T., Tanaka Y., Vaughan S., Ross R. R., 2004, *MNRAS*, 353, 1071  
 Fabian A. C. et al., 2009, *Nature*, 459, 540  
 Foreman-Mackey D., Hogg D. W., Lang D., Goodman J., 2013, *PASP*, 125, 306  
 Gallo L. C., 2006, *MNRAS*, 368, 479  
 Gallo L., 2018, in Revisiting Narrow-Line Seyfert 1 Galaxies and their Place in the Universe (NLS1-2018). 9-13 April 2018. Padova Botanical Garden, Italy. p. 34  
 García J., Kallman T. R., 2010, *ApJ*, 718, 695  
 García J., Dauser T., Reynolds C. S., Kallman T. R., McClintock J. E., Wilms J., Eikmann W., 2013, *ApJ*, 768, 146  
 García J. A., Fabian A. C., Kallman T. R., Dauser T., Parker M. L., McClintock J. E., Steiner J. F., Wilms J., 2016, *MNRAS*, 462, 751  
 Gonzalez A. G., Wilkins D. R., Gallo L. C., 2017, *MNRAS*, 472, 1932  
 Goodman J., Weare J., 2010, *Commun. Appl. Math. Comput. Sci.*, 5, 65  
 Goodrich R. W., 1989, *ApJ*, 342, 224  
 Grupe D., Mathur S., 2004, *ApJ*, 606, L41  
 Grupe D., Komossa S., Leighly K. M., Page K. L., 2010, *ApJS*, 187, 64  
 Haardt F., Maraschi L., 1991, *ApJ*, 380, L51  
 Jiang J. et al., 2018, *MNRAS*, 477, 3711  
 Jiang J., Walton D. J., Fabian A. C., Parker M. L., 2019a, *MNRAS*, 483, 2958  
 Jiang J., Fabian A. C., Wang J., Walton D. J., García J. A., Parker M. L., Steiner J. F., Tomsick J. A., 2019b, *MNRAS*, 484, 1972  
 Jin C., Done C., Ward M., Gierliński M., Mullaney J., 2009, *MNRAS*, 398, L16  
 Jin C., Ward M., Done C., Gelbord J., 2012, *MNRAS*, 420, 1825  
 Jin C., Done C., Ward M., Gardner E., 2017, *MNRAS*, 471, 706  
 Kara E. et al., 2015, *MNRAS*, 446, 737  
 Kara E., Alston W. N., Fabian A. C., Cackett E. M., Uttley P., Reynolds C. S., Zoghbi A., 2016, *MNRAS*, 462, 511  
 Kara E. et al., 2019, *Nature*, 565, 198  
 Kaspi S., Smith P. S., Netzer H., Maoz D., Jannuzi B. T., Givon U., 2000, *ApJ*, 533, 631  
 Komossa S., Xu D., Zhou H., Storchi-Bergmann T., Binette L., 2008, *ApJ*, 680, 926  
 McLure R. J., Dunlop J. S., 2004, *MNRAS*, 352, 1390  
 Marconi A., Axon D. J., Maiolino R., Nagao T., Pastorini G., Pietrini P., Robinson A., Torricelli G., 2008, *ApJ*, 678, 693  
 Mastroserio G., Ingram A., van der Klis M., 2019, *MNRAS*, 488, 348  
 Miniutti G., 2006, *Astron. Nachr.*, 327, 969  
 Osterbrock D. E., Phillips M. M., 1977, *PASP*, 89, 251  
 Panda S., Czerny B., Done C., Kubota A., 2019, *ApJ*, 875, 133  
 Parker M. L., Marinucci A., Brenneman L., Fabian A. C., Kara E., Matt G., Walton D. J., 2014, *MNRAS*, 437, 721  
 Parker M. L. et al., 2015, *MNRAS*, 447, 72  
 Pei Y. C., 1992, *ApJ*, 395, 130  
 Petrucci P. O., Ursini F., De Rosa A., Bianchi S., Cappi M., Matt G., Dadina M., Malzac J., 2018, *A&A*, 611, A59  
 Porquet D. et al., 2019, *A&A*, 623, A11  
 Reis R. C., Miller J. M., Reynolds M. T., Fabian A. C., Walton D. J., Cackett E., Steiner J. F., 2013, *ApJ*, 763, 48  
 Reynolds C. S., 2019, *Nat. Astron.*, 3, 41  
 Ross R. R., Fabian A. C., 1993, *MNRAS*, 261, 74  
 Shakura N. I., Sunyaev R. A., 1973, *A&A*, 24, 337  
 Svensson R., Zdziarski A. A., 1994, *ApJ*, 436, 599  
 Tang J.-J. et al., 2019, *MNRAS*, 484, 2575  
 Voges W. et al., 1999, *A&A*, 349, 389  
 Walton D. J., Nardini E., Fabian A. C., Gallo L. C., Reis R. C., 2013, *MNRAS*, 428, 2901  
 Wilkins D. R., Gallo L. C., Silva C. V., Costantini E., Brandt W. N., Kriss G. A., 2017, *MNRAS*, 471, 4436  
 Willingale R., Starling R. L. C., Beardmore A. P., Tanvir N. R., O'Brien P. T., 2013, *MNRAS*, 431, 394  
 Wilms J., Allen A., McCray R., 2000, *ApJ*, 542, 914  
 Wu X.-B. et al., 2015, *Nature*, 518, 512  
 Zoghbi A. et al., 2014, *ApJ*, 789, 56  
 Życki P. T., Done C., Smith D. A., 1999, *MNRAS*, 309, 561

## APPENDIX A: MCMC ANALYSIS

We check the constraints of all the parameters in the reflection model by using the MCMC algorithm. The XSPEC/EMCEE code by Jeremy Sanders based on the python implementation (Foreman-Mackey et al. 2013) and the MCMC ensemble sampler (Goodman & Weare 2010) was used. We use 50 walkers with a length of 250 000, burning the first 5000. A convergence test has been conducted and the Gelman–Rubin scale-reduction factor  $R < 1.3$  for every parameter. Figs A1–A5 show the output distributions of all the parameters. We do not find obvious evidence for parameter degeneracy. The uncertainty ranges of parameters given by our MCMC analysis are consistent with the measurements using the ERROR command in XSPEC.

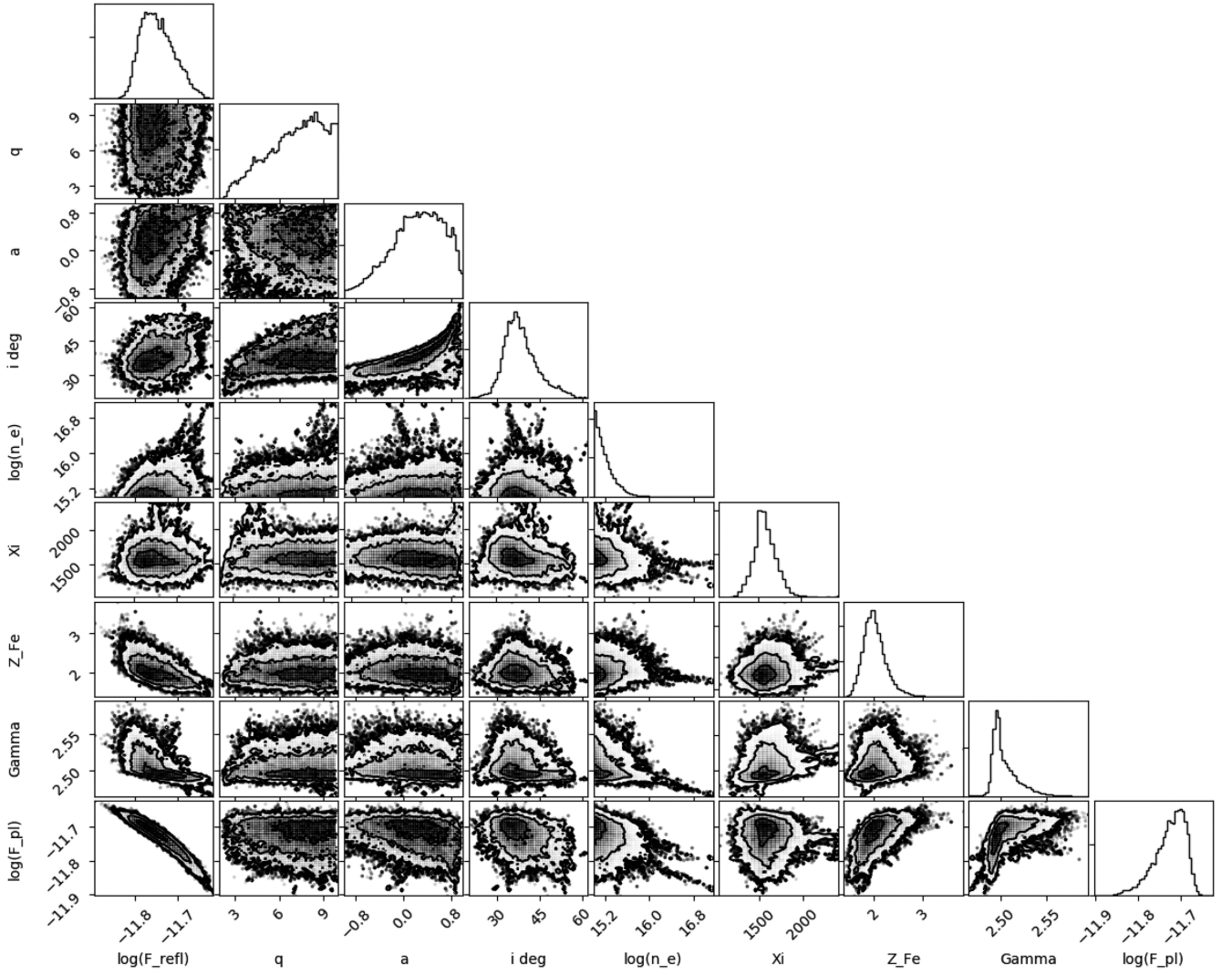


**Figure A1.** Output distributions for the MCMC analysis of the best-fitting models of the EPIC spectra of RBS 2041. Contours correspond to  $1\sigma$ ,  $2\sigma$ , and  $3\sigma$ . All the parameters are in the same units as in Table 2.

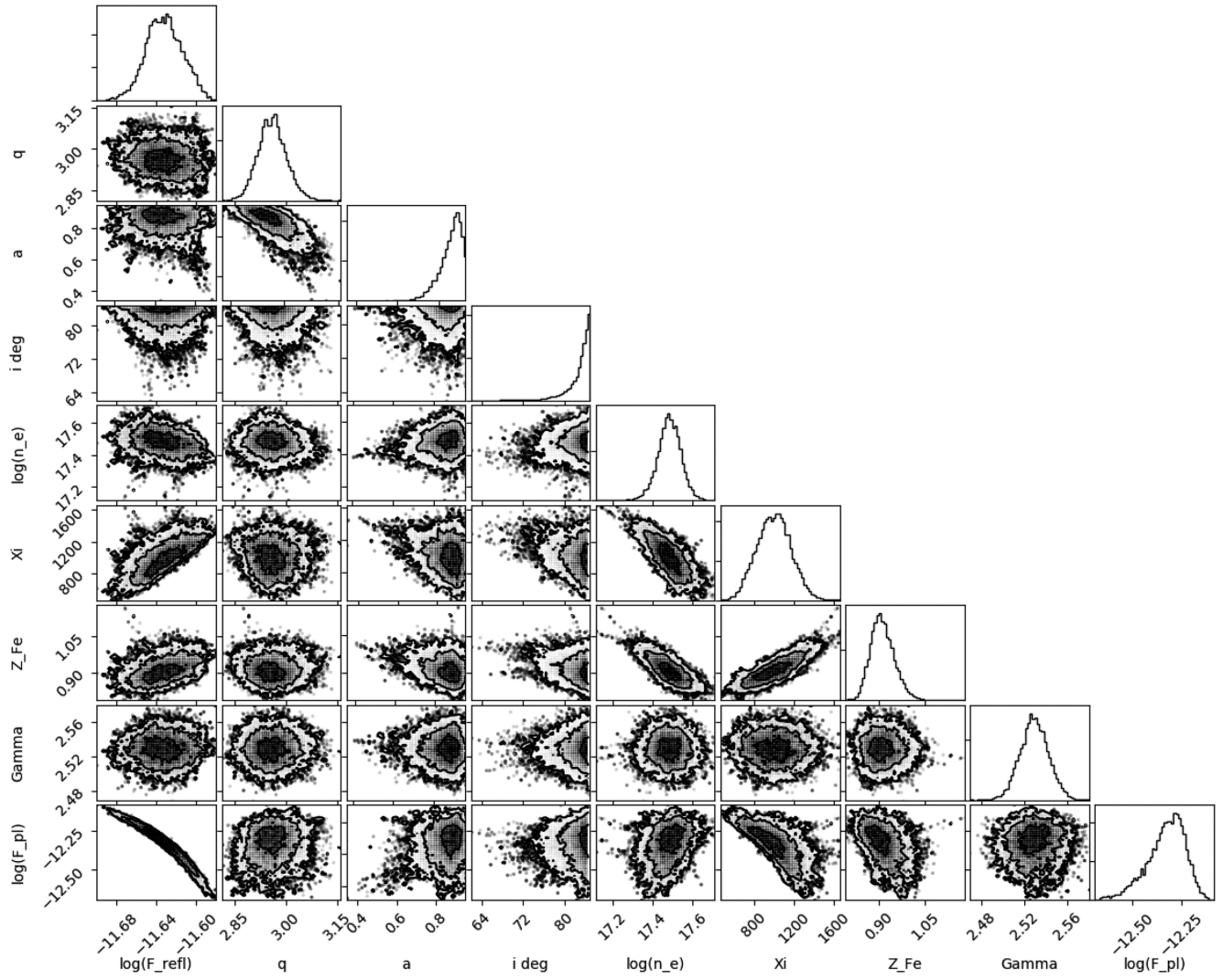


**Figure A2.** Output distributions for the MCMC analysis of the best-fitting models of the EPIC spectra of RX J0439.

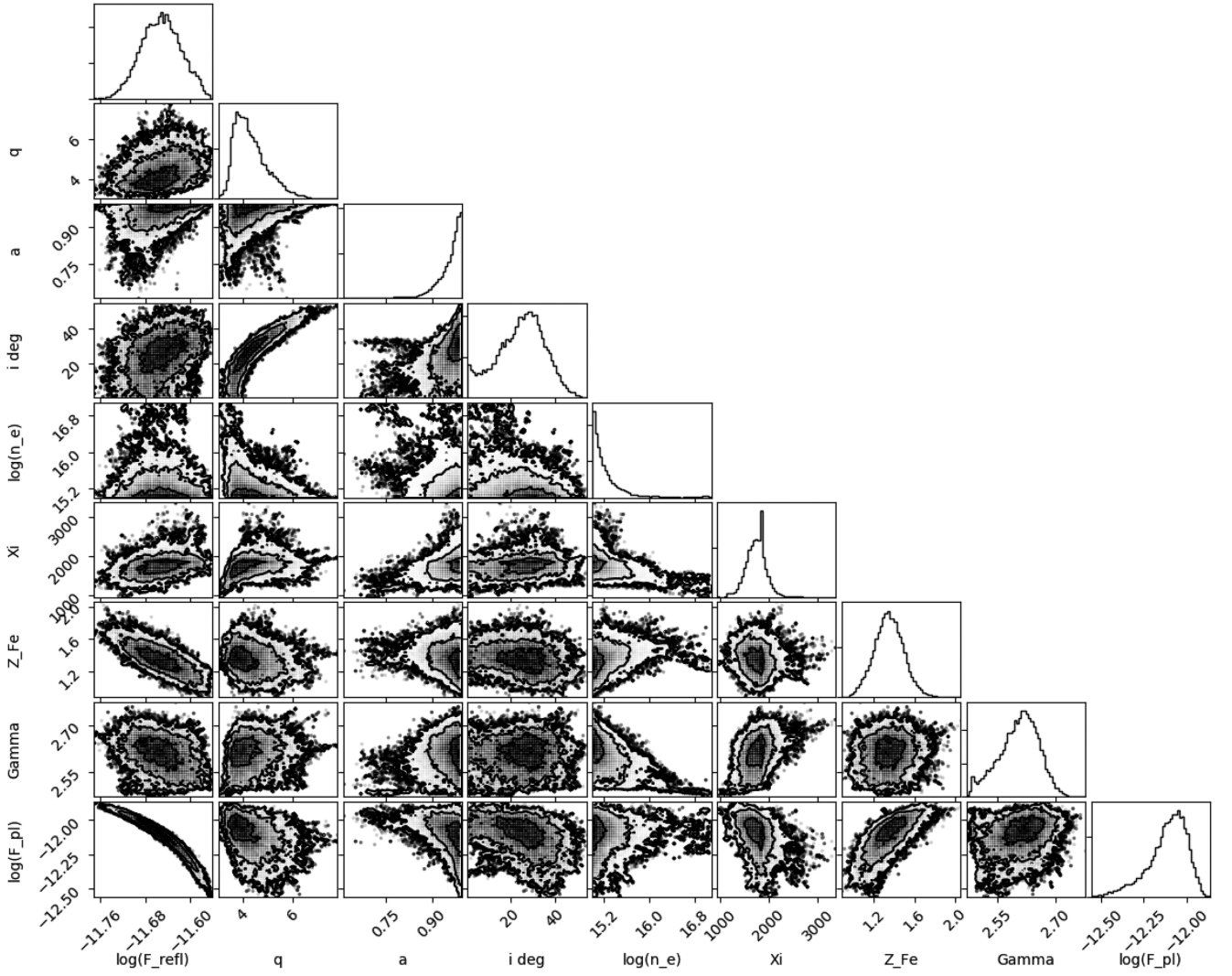


**Figure A3.** Output distributions for the MCMC analysis of the best-fitting models of the EPIC spectra of RX J0136.



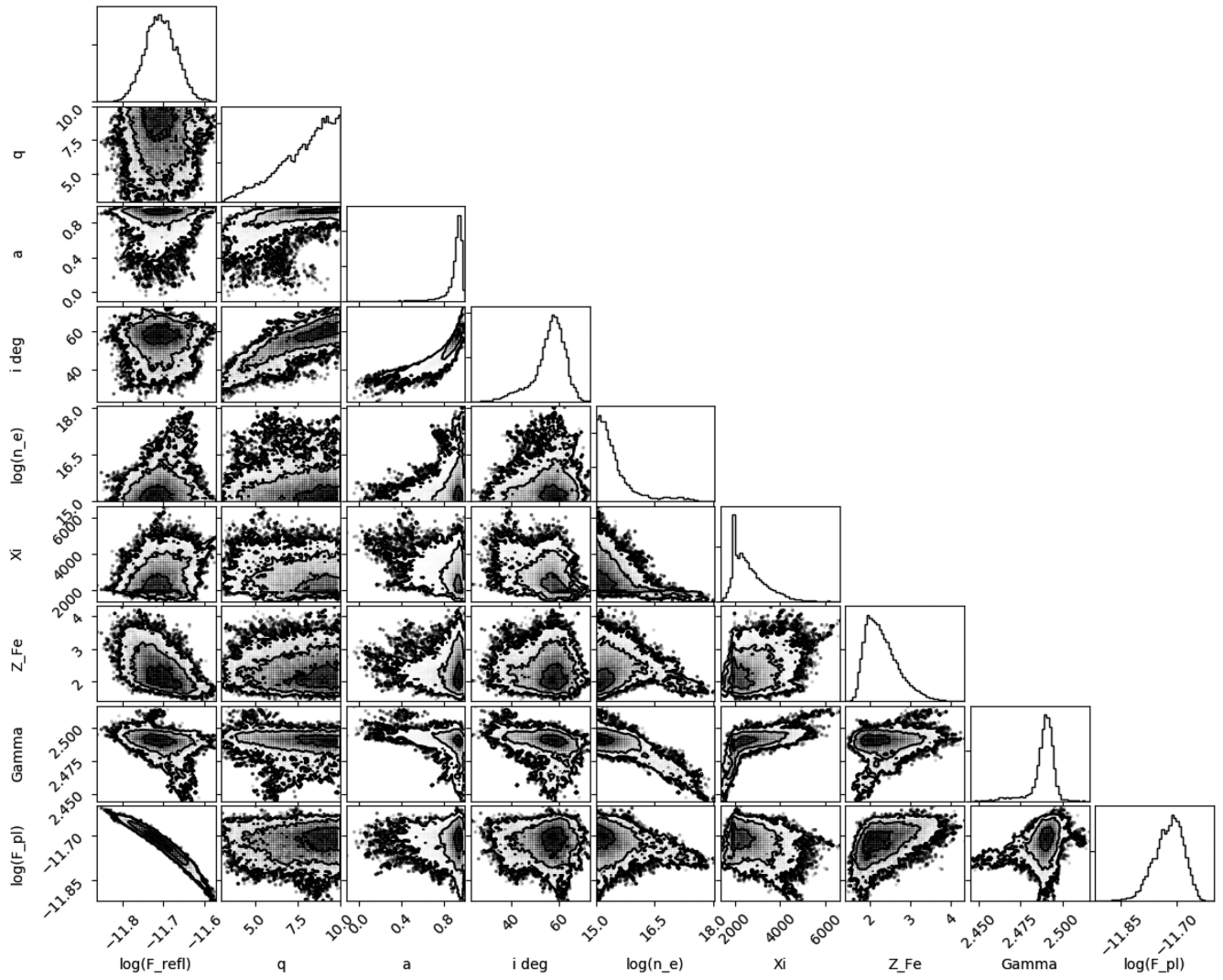


**Figure A4.** Output distributions for the MCMC analysis of the best-fitting models of the EPIC spectra of RX J1355.



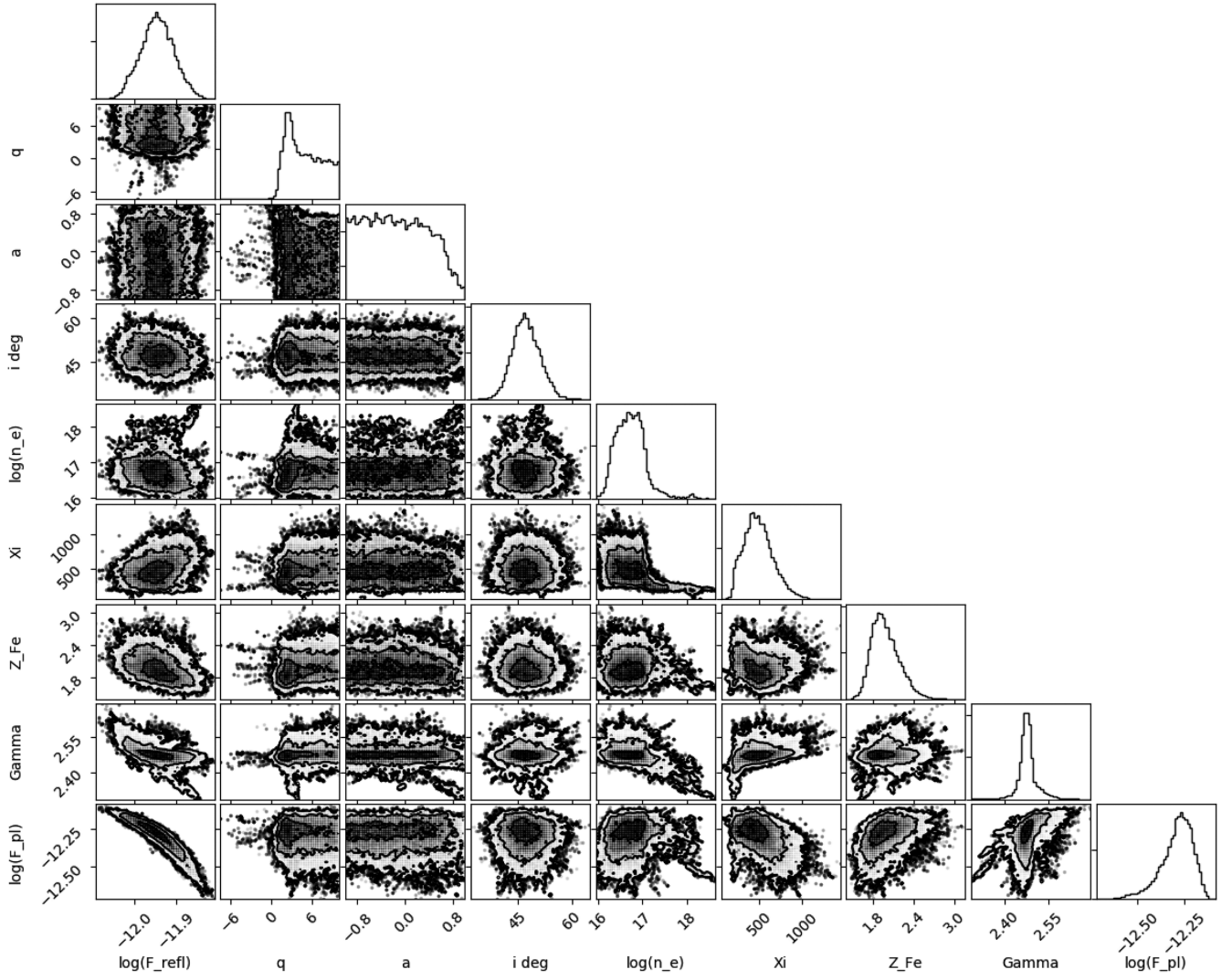


**Figure A5.** Output distributions for the MCMC analysis of the best-fitting models of the EPIC spectra of 1ES 0919.

This paper has been typeset from a  $\text{\LaTeX}$  file prepared by the author.